Progress In Electromagnetics Research C, Vol. 91, 265–277, 2019

Low-Power Microwave Induced Thermoacoustic Imaging: Experimental Study and Hybrid FEM Modeling

Ryan Jacobs[1], Mohand Alzuhiri[2], Mark Golkowski[1], and Yiming Deng[2, *]

Abstract—Microwave induced thermoacoustic imaging (TAI) is a hybrid imaging technique combining microwaves and ultrasound waves to achieve both superior spatial resolution and high image contrast. Here, we present results from a hybrid finite element model and an experimental setup using a microwave peak power of less than 5 kW (average power of only 4.5 W), significantly less than for comparable imaging performance in previous works. Microwave pulses with a duration less than 1 µs are used to excite ultrasound waves with a frequency higher than 1 MHz. Experimental measurements show agreement with simulation results using hybrid finite element modeling capturing microwave heating and acoustic wave propagation. Simulations suggest targets with a conductivity of approximately 0.9 S/m yield the strongest thermoacoustic signatures. Both B-mode images and time-reversal based reconstructed images are obtained and clearly demonstrate the enhanced contrast and high resolution by exploiting the dielectric absorption properties of microwaves and the sub-millimeter resolution of ultrasound. The use of a time reversal algorithm on recorded data demonstrates the effectiveness of TAI for biomedical applications. Standing wave patterns are identified in targets and their relation to the target characteristics and their effect on the resulted images are investigated. The novelty of this work is in lowering the microwave average power while still being able to detect induced acoustic signals, along with developing a numerical model to provide an insight into the imaging process and analyze anomalies in image reconstruction.

1. INTRODUCTION

Matter has the ability to support the propagation of different types of waves, many of which can be used to provide specific information and be exploited in imaging technologies for a wide range of applications from bio-medicine and structural health monitoring to surveillance. In all imaging technologies, researchers have striven to improve overall contrast and resolution with different measurement techniques and processing algorithms. Unfortunately, single wave imaging technologies are inherently limited by either the wavelength or the absorption depth of the radiated waves in media. Ultrasound imaging is a highly mature technology, in which medical diagnostic frequencies are typically 1 MHz–20 MHz [1]. However, for certain materials, the acoustic reflection and absorption coefficients do not exhibit significant variation, causing reduced contrast. For instance, in biomedical applications, poor contrast in ultrasound images is often encountered between soft tissue types (i.e. muscle vs. fat) due to similar acoustic impedances (or densities) of these two materials, which yield similar reflection coefficients. A primary advantage of microwave imaging is that contrast is based upon the permittivity and conductivity of the material being imaged. An active area of research for microwave imaging is early breast cancer detection. It is worth noting that the resolution of microwave imaging is not necessarily subject to the diffraction limit (based on the wavelength the diffraction limit is the angular separation of two sources that can be distinguished), depending on the measurement/processing technique used.

Received 1 October 2018, Accepted 21 March 2019, Scheduled 18 April 2019
* Corresponding author: Yiming Deng (dengyimi@egr.msu.edu).
[1] Department of Electrical Engineering, University of Colorado Denver, USA. [2] Department of Electrical and Computer Engineering, Michigan State University, USA.

However, traditional microwave imaging resolution is governed by diffraction when working in the far-field. Thus for most microwave frequencies used in biomedical applications that are below 12 GHz, the size of the smallest object that can be discerned is on the order of several centimeters or longer.

A novel way to overcome the limits of the aforementioned single-wave imaging is to synthesize different imaging modalities in what is known as multi-wave or hybrid imaging. The underlying concept is to combine the advantage of one type of wave, (i.e., one that yields high spatial resolution) with another wave (i.e., one that yields high contrast) [2]. In multi-wave imaging, the interrogating signal can be physically different from the observed signal. For example, in thermoacoustic imaging (TAI), the pulsed microwaves are the interrogating signal and the observed signals are ultrasound waves. The thermoacoustic effect we investigate uses pulsed microwaves, which are absorbed by the medium. When the medium absorbs bursts of microwave energy, it quickly heats and cools. This effect is known as thermoelastic expansion and can be observed by the compression waves that are generated.

The concept of TAI was first proposed by Bowen [3] and proof-of-concept measurements were subsequently shown [4]. One of the first publications showing significant imaging capability was the work described by Kruger et al. [5], who reported successful imaging of a kidney using a 25 kW peak power pulsed microwave source, a microwave frequency of 434 MHz, and transducer center frequency of 1 MHz. The reported data were acquired with an array of transducers using a liquid coupling medium. Contrast enhancement of thermoacoustic signals by use of microbubbles have been investigated experimentally [6] and theoretically [7] and shown to be effective. Other significant works include investigations of TAI as an early breast cancer detection method comparing radiograph, ultrasound, and TAI on four excised breast samples [8]. The challenges of thermoacoustic image reconstruction, and processing of data with a Time Reversal Mirror imaging technique are discussed by Chen et al. [9]. Absorption coefficients have been calculated and reduction of reconstruction errors by using a formula based on the least squares solution have been reported [10]. Various approaches to reconstruction using time-domain analysis, back projection, and adaptive reconstruction algorithm based on robust Capon beamforming have been published [11–13, 15, 16]. The use of electromagnetic (EM) waves in the range of 100–200 MHz to improve the penetration depth of TAI systems for human tissues is suggested by Eckhart et al. [14]. And the use of carbon nano tubes as a contrast agent to enhance the contrast of TAI for breast cancer detection is noted in Ref. [17].

A necessary feature for thermoacoutsic imaging to be viable in the biomedical space is that average EM power needs to be low so as not to cause thermal tissue damage or even discomfort. The experiment described herein uses a pulsed microwave system with maximum one microsecond (1 µsec) pulse full width at half maximum (FWHM) width, 4.5 kW peak power, and a repetition rate of 1 kHz. In terms of average power this translates to 4.5 W and is less power than other demonstrated approaches previously discussed [5, 6] and also the most recent published studies. Lou et al. [18] use a system with 2 MW–40 MW peak power, a pulse width of 0.1 µs, and repetition of 100 Hz. Razansky et al. [19] report a system that operates with peak power of multiple megawatts, a pulse width of 0.01 µs, and repetition of 100 Hz. Nan and Arbabian [20] introduce a continuous modulated power source with 120 W peak power and an average power that varies from 4.4 W–12 W depending on the modulation scheme. In terms of specific absorbtion rate (SAR), IEEE standard specifies the safety limits to be 10 W/kg in a controlled environment. A simulation study by Wang et al. shows that the safety limit is 15 kW peak power at 50 Hz repetition for a square pulse with a pulse width of 1 µs at 2.4 GHz [15] which is reduced to 750 W at 1 kHz. On the other hand, recently Nan and Arbabian [20] showed experimentally that the generated SAR levels from 4.4 W and 12 W are 2.47 W/kg and 8.74 W/kg consecutively indicating that a 4.5 W average power is within the IEEE safety standards.

The goal of this study is to explore the lower limits of microwave power necessary to obtain thermoacoustic images by performing experiments with less than 5 kW of peak power (4.5 W average power). Using lower microwave peak power and lowering the overall average power makes TAI a practical modality. The experimental results are interpreted with the aid of a new hybrid finite element 3D-2D electromagnetic-acoustic model to simulate the multiwave generation and investigate the imaging capabilities of the proposed system. The model is employed as an evaluation platform to test different experimental parameters on the excited TAI signal characteristics and behavior. The following sections provide a brief description of TAI signal generation theory, experimental setup, numerical modeling, image reconstruction, results, and discussion.

2. THERMOACOUSTIC THEORY

Thermoacoustic wave generation is an electromechanical phenomenon that results from thermoelastic expansion of a medium due to pulsed electromagnetic illumination. This thermal expansion results in a series of mechanical (acoustic) waves that are governed by the following wave equation [21, p. 785]

$$\bigtriangledown^2 p(\vec{r},t) - \frac{1}{c^2}\frac{\partial^2}{\partial t^2}p(\vec{r},t) = -\frac{\beta}{kc^2}\frac{\partial^2 T(\vec{r},t)}{\partial t^2} \tag{1}$$

where c, β, k are the sound speed, volume expansion coefficient, and the isothermal compressibility of the medium, respectively. $p(\vec{r},t)$ is the instantaneous pressure at coordinate $\vec{r}$. $T(\vec{r},t)$ is the temperature rise of the imaged object at time t and coordinate $\vec{r}$. The left side of the equation represents the acoustic wave equation, while the right side of the equation represents the thermoacoustic source. The thermoacoustic source depends on the second derivative of temperature in time, the volume expansion coefficient, and the heat capacity. The heat capacity and volume expansion coefficient are constants that depend on the medium properties. When the thermal confinement condition is met, the source part becomes equals to

$$\rho C_V \frac{\partial^2 T(\vec{r},t)}{\partial t^2} = H(\vec{r},t) \tag{2}$$

[21, p. 785] where ρ, C_V are the material density and specific heat capacity of the medium, and $H(\vec{r},t)$ is the heating function that represents the amount of dissipated energy per unit volume and time by the excitation pulse. In general, for a thermoacoustic system to work efficiently, two conditions should be met: thermal confinement and stress confinement [6]. The thermal confinement condition assumes that the excitation pulse is short enough so that the acoustic wave is excited before the occurrence of any significant heat conduction. This time is dependent on the time of thermal conduction of the dissipated power which can be approximated by $\tau_{th} = L_p/4D_T$, where L_p is the characteristic dimension and D_T is the thermal diffusivity of the object being imaged. The pulse width should be smaller than τ_{th} for any object to be imaged efficiently. On the other hand, stress confinement is related to the time for the stress to transit the heated region and can be approximated by $\tau_s = L_p/c$. For this condition to be met, the pulse width should be shorter than τ_s.

The heating function can be written as the product of two separate terms

$$H(\vec{r},t) = A(\vec{r})I(t) \tag{3}$$

where $A(\vec{r})$ is the absorbed energy per unit volume, and $I(t)$ is the temporal envelope of the excitation pulse. For microwave induced TAI in biological tissues, the magnetic losses are negligible. Therefore, the total losses are approximated to be the summation of conductivity and dielectric losses

$$A(\vec{r}) = \sigma(\vec{r})|E(\vec{r})|^2 + \omega\varepsilon''|E(\vec{r})|^2 \tag{4}$$

where σ, ε'', $E(\vec{r})$ are the material electrical conductivity, imaginary part of the permittivity, and root mean square value of the applied electric field inside the target. By combining these relations, the thermoacoustic equation is rewritten as

$$\bigtriangledown^2 p(\vec{r},t) - \frac{1}{c^2}\frac{\partial^2}{\partial t^2}p(\vec{r},t) = -\frac{\beta}{C_p}\frac{\partial H(\vec{r},t)}{\partial t} \tag{5}$$

where $C_p = \rho c^2 k C_V$ is the specific heat capacity of the medium under constant pressure.

3. EXPERIMENTAL SETUP

A photograph of the thermoacoustic experimental setup with a schematic of the system is shown in Figure 1. The experiment uses an Epsco PG5KB 5 kW peak power pulsed microwave source with an operating frequency of 2.4 GHz–2.5 GHz. Microwaves have a pulse length of 0.3 µs–1 µs. This study uses a submersible unfocused transducer (Olympus v306) with a center frequency of 2.25 MHz. A liquid coupling medium is required from the biological tissue sample to the transducer, and Safflower oil is used. Safflower oil has very low electrical conductivity which reduces the EM losses inside the tank and maximizes the losses in the target to yield a high contrast between the imaged target and

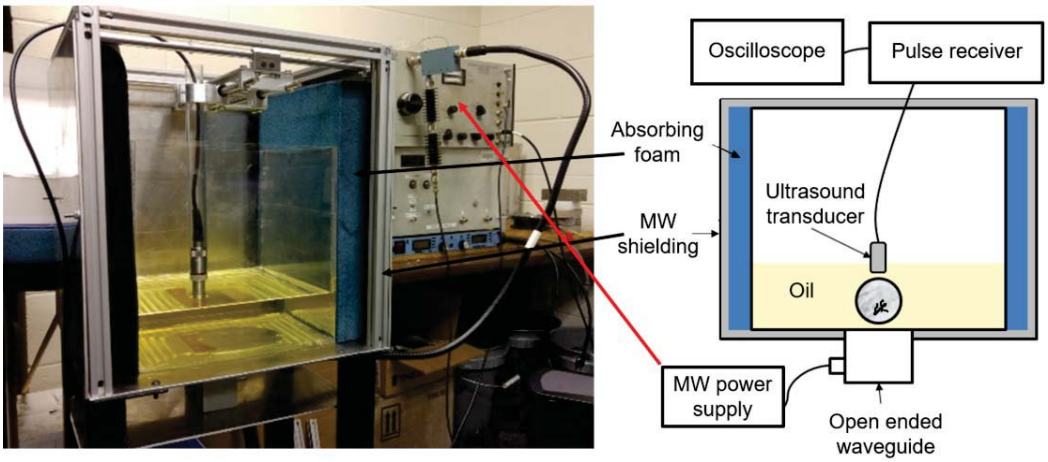

Figure 1. Photograph and schematic of experimental setup.

surrounding medium [6]. The permittivity of safflower oil is a close match to air, minimizing the amount of electromagnetic energy reflected across the two media. An acrylic tank is used to hold the oil since the dielectric properties of acrylic make it semi-transparent to microwave radiation. The transducer is fixed to a 2D scanner to perform raster scans in pulse/echo mode and in thermoacoustic mode. The transducer is moved in centimeter increments across the sample. All experiments are done in pulse/echo mode and in thermoacoustic mode for comparison. The peak power of the pulsed microwaves is set to 3.5 kW–4.5 kW. To improve the signal to noise ratio (SNR), averaging was used in addition to a 60 dB pre-amplifier. The acoustic signal is acquired with a high speed digital oscilloscope (R&S RTO 1014). The whole experimental setup is triggered by using a function generator with a repetition frequency of 1 kHz. This gives an average power of less than 5 W.

4. NUMERICAL MODELING

A finite element numerical model was created with COMSOL Multiphysics [22] to optimize the experimental setup through parametric studies and development of reconstruction algorithms, namely time reversal. The model is divided into an EM and an acoustic module that are coupled sequentially. The EM module simulates the EM waves propagation according to

$$\nabla \times \mu_r^{-1}(\nabla \times \boldsymbol{E}(\vec{r})) - k_0^2 \left(\varepsilon_r - \frac{j\sigma}{\omega\varepsilon_0}\right) \boldsymbol{E}(\vec{r}) = 0 \tag{6}$$

[22] where μ is the magnetic permeability, ε_r the electric relative permittivity, ω the wave angular frequency, and k_0 the propagation constant. The EM absorption density, $H(\vec{r}, t)$, inside the sample is calculated according to Equation (3) where it mainly depends on two parameters; the intensity of the electric field (E) and the electrical conductivity (σ). $I(t)$ represents the temporal profile of the EM energy that is injected into the model as a Gaussian function. The ultrasound excitation (Q_t) is defined by

$$Q_t = \frac{\rho\beta}{C_p}\frac{\partial}{\partial t} H(\vec{r}, t) \tag{7}$$

where the heat change is differentiated with respect to time. This ultrasound source is then inserted as a monopole source on the right of the acoustic wave equation as

$$\frac{1}{\rho c^2}\frac{\partial^2 p}{\partial t^2} + \nabla \cdot \left(-\frac{1}{\rho}(\nabla p)\right) = Q_t. \tag{8}$$

After the excitation of the acoustic source, the thermoacoustic wave propagation inside the domain is simulated, and the final data are recorded for evaluation or reconstruction.

4.1. Model Geometry

The experimental geometry that was described in Section 2 is simulated with different types of phantom samples. We simulate a WR-340, D band waveguide with cross-section dimensions of 86.36 mm × 43.18 mm and excite it with a 2.45 GHz EM signal. The waveguide is modeled as an air filled rectangular enclosure with perfect electric conductor boundaries. The waveguide is excited with a wave port that couples a single transverse electric mode (TE_{10}) and is connected to an acrylic tank that is filled with safflower oil for acoustic coupling. The tank has a wall thickness of 3 mm.

EM wave propagation is simulated inside the waveguide and the safflower oil in the tank. The simulation domain is terminated with absorbing boundaries at the top and side of the acrylic tank. A perfect electric conductor boundary is assumed at the bottom of the tank because the experimental setup base of the tank is made of aluminum which has a very high conductivity of (10.79×10^6 S/m) [23] at microwave frequencies. The acoustic wave excitation and propagation simulation is performed in a smaller region of the geometry around the target due to the slow speed of sound. The simulated acoustic domain is terminated with an absorbing boundary condition.

4.2. Model Validation

A circular target with biological tissue properties is employed to validate the model by comparison to experimental work [6] and simulation results [7]. The model simulates the generation of thermoacoustic signals by a circular target that has a radius of 6 mm, and this target is made of ethylene glycol with different concentrations of air microbubbles. The different concentrations of air micro-bubbles introduce different electric and mechanical properties inside the imaged object. Table 1 provides details of the change in material properties with bubble concentration and shows that both electrical conductivity and permittivity of the imaged target decrease with the increase of the air micro-bubbles concentration

Table 1. Change of permittivity, conductivity and sound speed with the change of micro-bubbles concentrations [6].

Concentration	σ (S/m)	ε_r	Sound speed m/s
0%	2.32	14.03	1660.7
20%	1.33	9.66	1729.8
30%	1.11	8.34	1805.6
35%	0.95	7.38	1922.6
40%	0.84	6.86	2049.4

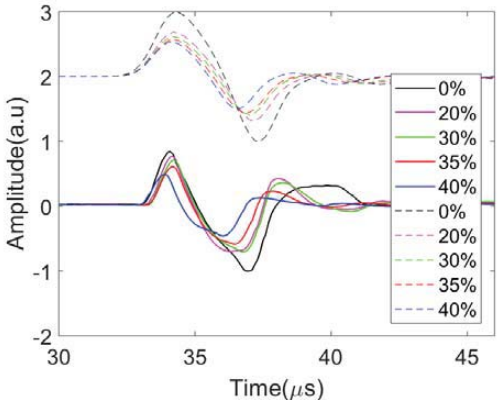

Figure 2. Thermoacoustic simulation of different micro-bubbles concentrations suspended in ethylene glycol(dashed lines) compared to experimental results (solid lines) [6].

while the sound speed increases.

The imaged target is immersed in safflower oil and a virtual acoustic transducer is aligned in a position normal to the imaged sample surface. The EM source has a center frequency of 2.45 GHz, and the wave is modulated with a Gaussian pulse. Figure 2 shows the results of simulating these five different materials and compares the results with experimental results that were previously published [6]. The results show that the amplitude of the signal decreases with the increase of the air micro-bubbles concentration (decrease of conductivity) and this is related to the decrease of the EM losses inside the material. The model also shows that the signal wavelength is decreased with the increase of air micro-bubbles concentration and this is related to the increase of sound speed.

5. IMAGE RECONSTRUCTION

Different algorithms have been proposed to for image reconstruction from thermoacoustic signals, and their performance varies depending on the target material properties and acquisition geometry [9–11]. In our experiment, image reconstruction is performed by using time-reversal due to its simplicity and robustness [24]. Time reversal is based on the reciprocity of the wave equation by assuming that the source of the signal can be uniquely reconstructed by inverting time and re-transmiting the signal to the same domain. According to Huygens principles, for any initial source that has a bounded support, there is a finite time for the wave to leave the domain [24]. Therefore, a solution p vanishes inside the domain after a finite amount of time T. After the time T, a zero initial value can be imposed to the domain, and the wave can be retransmitted to the domain in reversed timing sequence to reconstruct the source. The re-transmission of the wave again into the media with the same received pressure and boundary conditions results in the reconstruction of the initial source [25]. The reconstruction process is implemented by using two different software packages to ensure the acuracy of the model. Results from a hybrid COMSOL model where compared to results generated using Matlab k-Wave toolbox [26].

Optimal reconstruction of thermoacoustic tomography images requires that the target is surrounded by 360 degrees of transducers [27, p. 834]. This is an expensive approach and difficult to implement in practice. In-order to reconstruct a point completely inside a homogeneous media, any line that passes through that point should intersect with the transducers plane at least one-time. The case becomes more complicated in the case of inhomogeneous media because the waves are deflected due to medium inhomogeneity. To show this effect, a simulation with different transducer positions is performed. The first simulation uses an array of transducers that are positioned on the top of the simulated geometry (line array). The second simulation adds another array of transducers on the left side of the simulation domain (L-shaped). Figure 3 shows the reconstruction results with the different transducers positions. The simulated geometry is shown in Figure 3(a) while Figure 3(b) and Figure 3(c) show the reconstruction results with line and L-shaped arrays consecutively. Figure 3(d) shows a comparison of the reconstruction along the dotted line at $x = -0.5$ mm in both cases and compares them with the original simulated object (negative pressure is neglected). The results show that the edges that are normal to the transducers' plane are reconstructed clearly while the other edges are blurred. When the L-shaped array is used, the edges of the rectangular object are reconstructed precisely while the circle still exhibits some blurred edges because the array elements are not normal to those edges.

6. CASE STUDIES AND DISCUSSION

A variety of experimental parameters can affect thermoacoustic signal intensity and characteristics. In this section, different scenarios are studied to show the effect of the excitation signal and imaged object properties on the thermoacoustic signal characteristics.

6.1. Simulation Study of Image Reconstruction with Time Reversal

Three objects with different shapes are placed in safflower oil to study the reconstruction with time reversal as shown in Figure 4(a). The samples are a circle with a radius of 1 mm, square with a side length of 2 mm, and a rectangle with dimensions of 1.5 mm by 3 mm. The forward model employs the

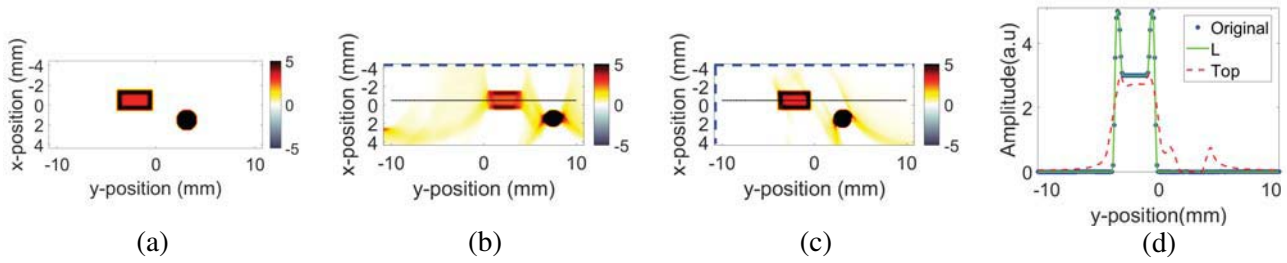

Figure 3. Effect of transducer orientation on image reconstruction. (a) The simulated geometry. (b) Reconstruction with transducers aligned linearly along the top. (c) Reconstruction with transducers aligned in L shape along the top and left boundaries. (d) A comparison of the amplitude along the dotted line at $x = -0.5$ mm.

same setup that was explained previously. The model is excited with a pulse that has a carrier frequency of 2.45 GHz and a Gaussian shape with a pulse width of 40 nanoseconds. All the samples are set to have the same electrical conductivity of 0.4 S/m, a relative permittivity of 9, and a sound speed of 1537 m/s. The acoustic transducers are represented by an array of point-like transducers that are placed at the top of the simulation domain. Figure 4(b) shows a uniform EM loss distribution inside the samples which indicates that the sample regions can be reconstructed well. The same forward acoustic simulation model is recreated by using the K-wave toolbox, and the signals are retransmitted in a reverse time sequence. Time reversal results are shown in Figure 4(c) and a thresholded version of it is shown in Figure 4(d). The positions and sizes of the objects are reconstructed successfully. The case is the same for the edges that are normal to the transducer plane while we can see that the horizontal edges are blurred due to the orientation of the detection plane.

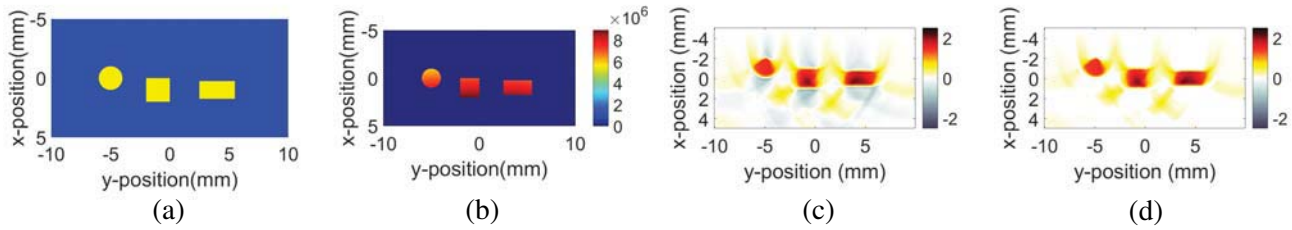

Figure 4. Reconstruction with time reversal. (a) Model geometry. (b) EM losses distribution. (c) Time reversal reconstruction. (d) Image after neglecting negative values.

6.2. Effect of Material Conductivity

In this study, the change of physical properties of the material in Table 1 is neglected, and only the conductivity is changed. The results are shown in Figure 5(a), where increasing the conductivity increases the amplitude of the generated thermoacoustic signals. This behavior is a result of the increase of losses of EM waves according to Equation (4). However, increasing the conductivity above certain threshold reduces the skin depth of the imaged object, which will be discussed later. The study is extended to 2D to show the effect of these results on the final image. Two circular objects with diameters of 1 mm and electrical conductivity of 0.75 S/m are embedded in another biological tissue that has lower conductivity (0.4 S/m). The results of EM losses distribution in Figure 5(b) show a high contrast between the objects and the medium that they are embedded in due to the electrical conductivity differences. Figure 5(c) shows the reconstructed results while 5(d) shows a comparison between the EM losses and the reconstructed profiles of the imaged objects. EM absorption thus determines the image contrast and overall signal strength.

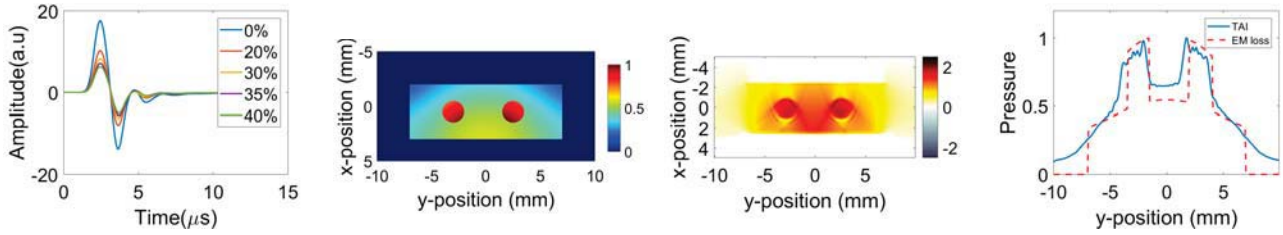

Figure 5. The effect of conductivity on TAI images. (a) 1-D TAI signal variation with change of conductivity. (b) Normalized EM losses distribution. (c) Time reversal reconstruction. (d) A 1D comparison between the EM losses and reconstructed TAI images at $x = 0$.

Since the conductivity plays an important role in controlling the magnitude of the generated thermoacoustic signals, the optimal conductivity is investigated using the numerical model and simple plane wave analytical expressions. A sample with dimensions of 30 mm by 120 mm is simulated and a parametric sweep is performed over a wide range of electrical conductivities to calculate the amount of the EM loss inside the imaged sample. The loss calculation is performed by taking a line integral from the surface of the sample to 10 mm from the sample surface. The results of the study are shown in Figure 6. The figure shows the EM power losses for ε_r equals to one and three. The dashed lines are the results from a COMSOL model solution. The solid lines represent a direct analytical solution assuming plane wave propagation and normal incidence. In this case, the losses are calculated directly from evaluating the below integral for different values of σ and ε_r

$$W_{loss} = \sigma E^2 T^2 \int_0^{0.01} e^{-2\alpha z} dz \tag{9}$$

where T and α are the transmission and the attenuation coefficients given by

$$\alpha = \omega \sqrt{\frac{\mu\varepsilon}{2}\left[\sqrt{1+\left(\frac{\sigma}{\omega\varepsilon}\right)^2}-1\right]} \tag{10}$$

$$T = \frac{2\eta_2}{\eta_2+\eta_1} \quad \text{where} \quad \eta = \sqrt{\frac{\mu}{\varepsilon}} \tag{11}$$

The integration represents the total dissipated power assuming a normally incident wave and neglecting any reflections inside the system. We started by testing the conductivity values around 1 S/m (the range of conductivity for different human biological tissues) and continued increasing the

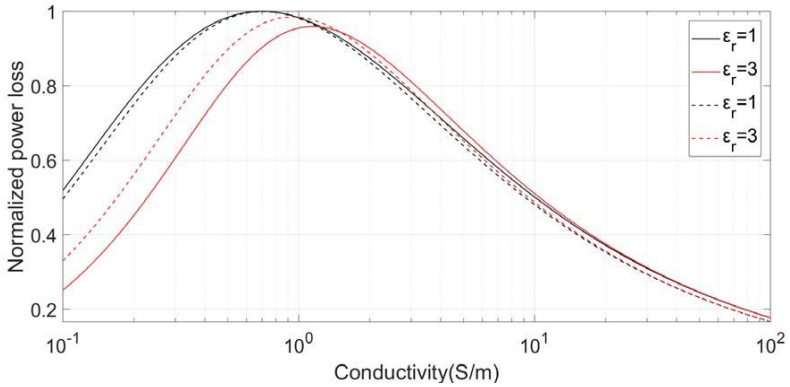

Figure 6. EM losses inside the imaged sample over wide range of σ. (a) Simulation(dashed lines). (b) Analytical solution(solid lines).

conductivity until the power loss decreased below 20% of its maximum value at 100 S/m. Results show that the EM power losses inside the target increase as we increase the conductivity to a certain level and then start to drop for higher conductivity. In the beginning, the increase can be explained according to Equation (1), where the loss is proportional to the electrical conductivity. After that, the skin depth of the sample starts to decrease until the EM wave is no longer able to penetrate through the sample. From the results, it can be inferred that the conductivity plays an important role in increasing the intensity of the thermoacoustic signal, but a high conductivity reduces the skin depth of the EM waves and results in thermoacoustic waves that are only generated from the surface of the imaged sample. The simulation agrees well with the analytical solution when $\varepsilon_r = 1$, but the peak deviates when $\varepsilon_r = 3$. This can be related, as mentioned earlier, to the assumption of normal incidence, plane wave propagation, and to the effect of reflections in the system that are not considered in the analytical formulations.

6.3. Effect of EM Pulse Width

In this study, different microwave pulses are transmitted with different pulse widths while the simulation environment is kept unchanged. The Gaussian pulse width is changed from 0.3 µs–0.9 µs. The results are shown in Figure 7(a) where it can be seen that increasing the pulse width directly increases the wavelength of the generated thermoacoustic signal. This means that decreasing the microwave pulse width directly enhances the resolution of the thermoacoustic images. The simulation is repeated to simulate the reconstruction of a complete sample with different EM pulse widths with a standard deviation of 4 microseconds. The results are shown in Figure 7(b). Comparing these results with the reconstruction results in Figure 4(d) it can be seen that the spatial resolution of the reconstructed images is decreased with the increase of the EM pulse width due to the increase of the acoustic signals wavelength.

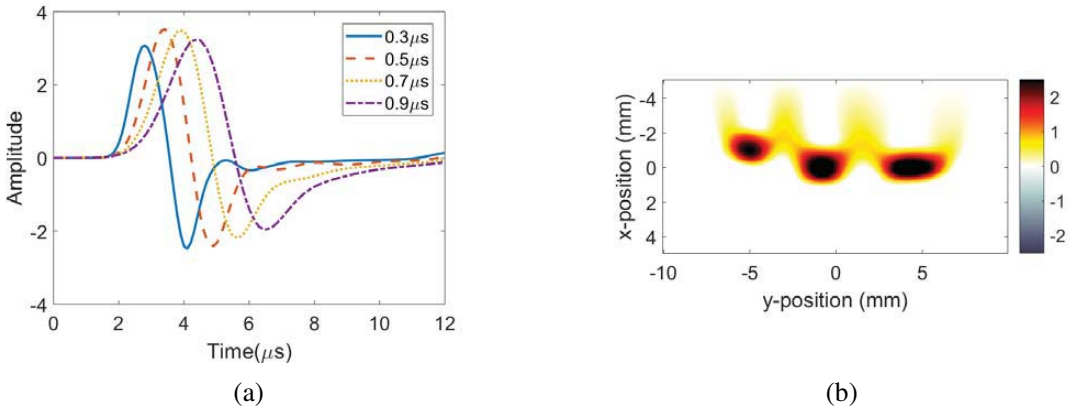

(a) (b)

Figure 7. The effect of EM pulse width on the reconstructed image. (a) Model geometry. (b) Image reconstruction with pulse width = 4 µs.

7. EXPERIMENTAL RESULTS

7.1. Experimental Setup Validation

For verification that the experimental setup was working properly, 1D data were initially recorded as shown in Figure 8. Here the ultrasound transducer is set at two different depths and records thermoacoustic signatures with different times of arrival. The time shown is the total round trip flight time. The pulse/echo mode data in the top panel of 8 clearly show the acoustic reflection of the first target at 44 µs and the acoustic reflection of the second target at 51 µs. Since the pulse/echo mode signal has a round trip flight double that of a thermoacoustic signal we expect to see a thermoacoustic signal at 22 µs and 25 µs, respectively. The thermoacoustic signals shown in the bottom panel of Figure 8 are observed at the expected arrival times and are seen to have longer time signatures as compared to the abrupt pulse/echo mode signatures.

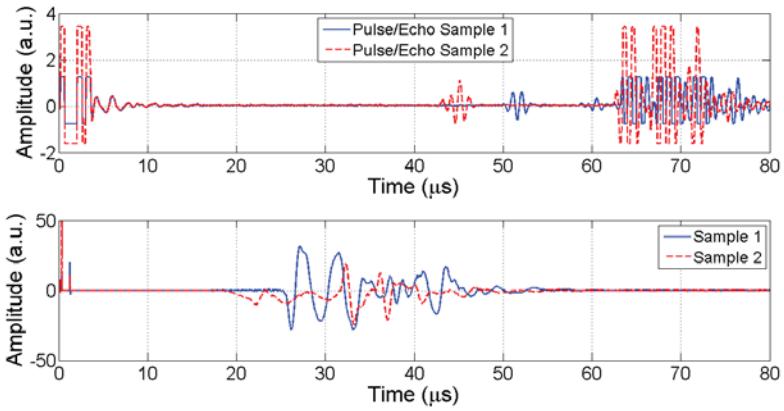

Figure 8. Top: Recorded ultrasound signal in pulse echo mode with the transducer at different depths to the sample. Bottom: Thermoacoustic signal with the transducer at different depths to the sample.

7.2. 2-D Thermoacoustic Imaging

Being able to accurately estimate the arrival time of the thermoacoustic signal we move on to performing raster scans across the target with a single element transducer. Figure 9(a) shows an ultrasound B-mode scan of a tissue sample with a 4 mm wire embedded into it. In the B-mode scan, the embedded wire can clearly be seen below the surface of the tissue sample. Figure 9(b) (Figures 9(c) and 9(d) are discussed later) shows the sample tissue sample with a thermoacoustic B-mode scan. To test how different conductivities affect thermoacoustic B-mode scans a composite tissue sample was created by taking a homogeneous sample, cutting out the center, soaking the center in salt water for 24 hours and placing it back into the remaining tissue sample. This creates a sample with two unknown but different conductivities σ_1 and σ_2 as shown in Figure 10. The conductivity of the salt-soaked center, σ_2 is shown to be significantly larger than σ_1. Figure 10(a) shows the ultrasound B-mode scan. Here it is difficult to define the difference between the two conductivities. Figure 10(b) (Figure 10 (c) and Figure 10(d) are discussed later) show the thermoacoustic B-mode scan where the difference between low and high conductivities of the sample can be easily identified, highlighting the unique advantages of the thermoacoustic approach.

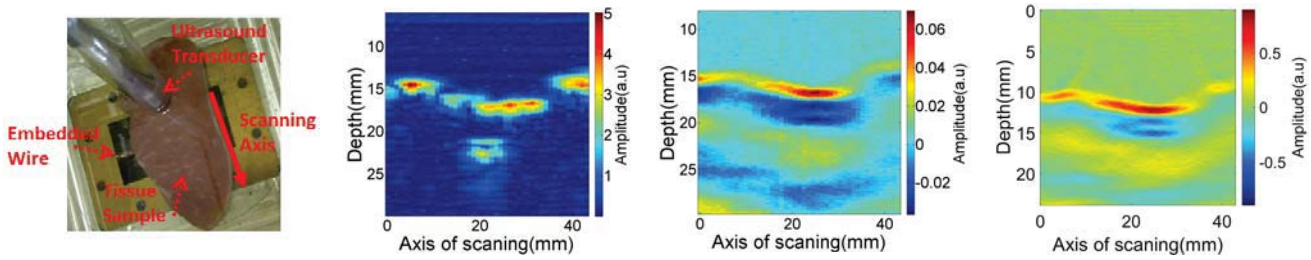

Figure 9. (a) Picture of tissue sample with wire embedded into sample. (b) B-mode Ultrasound image. (c) Theremoacoustic image. (d) Time reversal reconstruction.

The time-reversal algorithm that was described in Section 5 was applied to the reconstruction of the experimental data. A geometry similar to the experimental setup is created in the K-wave simulation tool box with a perfectly matched layer (PML) boundary conditions. The simulation sound speed is set to be equal to the average of sound speed in safflower oil and the imaged sample (1500 m/s), and the recorded data is interpolated to match the time steps of the simulation. To improve the signal-to-noise ratio, each measured transducer signal is filtered by a median filter with an order of 20 in the

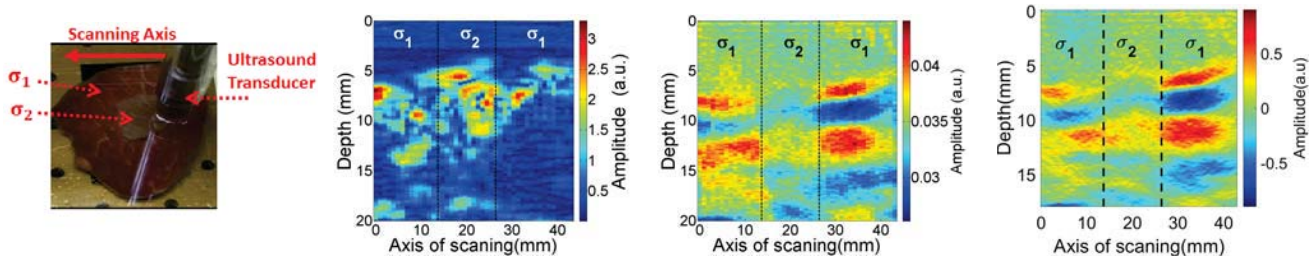

Figure 10. Scan of tissue sample with inhomogeneous conductivity. (a) Picture of composite sample. (b) B-mode ultrasound image. (c) Theremoacoustic image (d) Time reversal reconstruction.

pre-processing stage. After filtering the signals, they are inserted in the simulation domain from the top as an array of omnidirectional transducers. The results of the reconstruction are shown in Figures 9(d) and 10(d). The results show that the time reversal enhances the horizontal edges of the reconstruction and gives a better localization for the wire in Figure 9. On the other hand, the application of time reversal in the case of Figure 10 results in blurring of vertical edges. This degradation is related to two factors. The first factor is that the system is using a top scanning platform, which means that the image is reconstructed with an incomplete set of information about the imaged object. The second factor is the use of directional transducers in the experimental data collection, while the time-reversal algorithm assumes an omnidirectional point source. In the experimental results, periodic patterns of hot and cold regions are noticed in the imaged samples. These periodic patterns are present in all the biological samples images, and they have no relation to the samples internal structure. To investigate these patterns, the numerical model is configured to simulate a phantom target that has similar electrical properties to muscle tissues. The model simulates the EM wave propagation and interactions inside the imaged sample. The muscle tissues have an approximate relative permittivity of 80 and a conductivity of 0.9 S/m at microwave frequency [28]. Figure 11 shows the simulation results for modeling a uniform sample, a sample with a wire embedded inside it and a sample that has a highly conductive object ($\sigma = 10$ S/m) in the middle of two normal tissues to mimic the case of inserting the sample with the salt. The results show that standing wave patterns are created inside the samples and are introducing patterns of hot and cold spots inside the sample. The standing wave creation is related to the EM impedance mismatch at the boundary between the imaged sample and the safflower oil due to their different electrical permittivity.

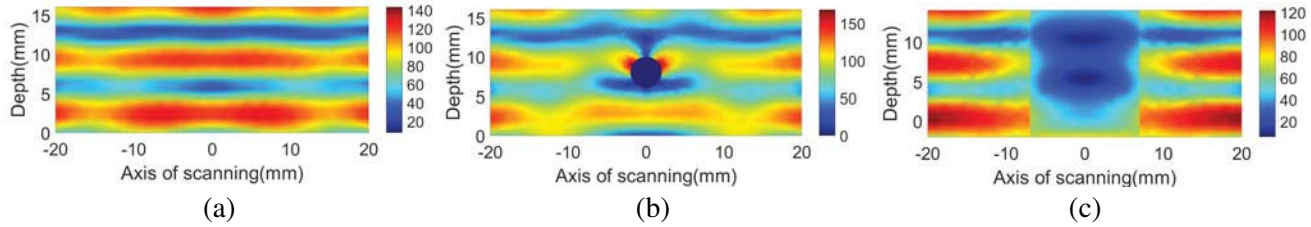

Figure 11. Simulation of electric field distribution in muscle tissue. (a) Uniform rectangular Tissue. (b) Wire embedded in a uniform sample. (c) Highly conductive object embedded in a uniform sample.

8. CONCLUSION

Thermoacoustic imaging is a hybrid methodology that combines the advantages of microwave imaging and ultrasonography. Here we reported experimental results using a less than 5 kW peak (4.5 W average power) power which is at least 4 kW–4.5 kW lower than past published works [3–11]. We are able to use this low power to achieve satisfactory contrast and resolution, with thermoacoustic imaging providing superior contrast to ultrasound imaging in the case of soft biological tissue samples with

similar acoustic properties but different conductivities. A comprehensive numerical model was created to simulate the signal generation of thermoacoustic imaging systems and compare to experimental results. The model shows that the acquired thermoacoustic images represent the EM loss distribution inside the imaged target. The signal is maximized for conductivities near 1 S/m after which the skin depth of the electromagnetic wave decreases to an undesirable length due to the high conductivity of the medium. In the same manner, increasing the electromagnetic frequency generates a stronger acoustic signal due to greater absorption of the medium but this also decreases the skin depth of the electromagnetic wave into the medium. It was also found that the EM pulse width has a direct effect on the acoustic frequency (i.e., decreasing or shortening the pulse width increases the acoustic frequency and results in a higher-resolution images). The time reversal reconstruction algorithm was used for the reconstruction of the TAI due to its robustness. This method of image reconstruction was implemented successfully to reconstruct both simulation and experimental data. For simulation, different case studies were implemented for different target shapes and transducer orientations. Different biological samples were tested with different conductivities, shapes, and sizes. The surface boundaries of the samples are easily identifiable in the reconstructed data. Future work will include an investigation of possible methods for the reduction or elimination of the standing waves identified inside the samples under test. Since the current experimental work was performed mainly on uniform samples, the study of the effect of heterogeneity is planned for the next phase of the work. Different non-contact coupling techniques should be explored to possibly identify a more efficient way to acquire the acoustic signal. Our findings suggest the use of TAI for advanced manufacturing, where improved assessment of multi-materials joining and composites is possible, as well as in non-destructive evaluation and biomedical applications.

ACKNOWLEDGMENT

The authors would like to thank the undergraduate research opportunity program (UROP) at University of Colorado Denver for a 2011 grant to student PI Ryan Jacobs that provided the initial funding for this work. The authors thank Gas Technology Institute for their support under the U.S. DOT grant DTPH56-15-T00007 and GTI grant S658 for numerical modeling and data reconstruction studies. The authors also thank Super Pulse in Ithaca, NY for donation of a high voltage power supply.

REFERENCES

1. Chan, V. and A. Perlas, "Basics of ultrasound imaging," *Atlas of Ultrasound-Guided Procedures in Interventional Pain Management*, 13–19, Springer New York, 2011.
2. Fink, M. and M. Tanter, "Multiwave imaging and super resolution," *Phys. Today*, Vol. 63, 28–33, 2010, 10.1063/1.3326986.
3. Bowen, T., "Radiation-induced thermoacoustic soft tissue imaging," *1981 Ultrasonics Symposium*, 817–822, Chicago, IL, USA, 1981.
4. Bowen, T., R. L. Nasoni, A. E. Pifer, and G. H. Sembroski, "Some experimental results on the thermoacoustic imaging of tissue equivalent phantom materials," *1981 Ultrasonics Symposium*, 823–827, Chicago, IL, USA, 1981.
5. Kruger, R. A., K. K. Kopecky, A. M. Aisen, D. R. Reinecke, G. A. Kruger, and W. L. Kiser, "Thermoacoustic CT with radio waves: A medical imaging paradigm," *Radiology*, Vol. 211, 275–278, 1999.
6. Mashal, A., J. H. Booske, and S. C. Hagness, "Toward contrast-enhanced microwave-induced thermoacoustic imaging of breast cancer: An experimental study of the effects of microbubbles simple thermosacoustic targets," *Phys. Med. Biol.*, Vol. 54, 641–650, 2009.
7. Deng, Y. and M. Gołkowski, "Innovative biomagnetic imaging sensors for breast cancer: A model-based study," *J. Appl. Phys.*, Vol. 111, 07B323, 2012.
8. Xu, M., G. Ku, X. Jin, L. V. Wang, B. D. Fornage, and K. K. Hunt, "Breast cancer imaging by microwave-induced thermoacoustic tomography," *Proc. SPIE 5697, Photons Plus Ultrasound: Imaging and Sensing 2005: The Sixth Conference on Biomedical Thermoacoustics, Optoacoustics, and Acousto-optics*, Vol. 45, May 05, 2005.

9. Chen, G. P., et al. "The prototype of microwave-induced thermo-acoustic tomography imaging by time reversal mirror," *Journal of Electromagnetic Waves and Applications*, Vol. 22, 11–12, 1565–1574, 2008.
10. Ammari, H., et al., "Quantitative thermo-acoustic imaging: An exact reconstruction formula," *Journal of Differential Equations*, Vol. 254, No. 3, 1375–1395, 2013.
11. Xu, Y., M. Xu, and L. V. Wang, "Exact frequency-domain reconstruction for thermoacoustic tomography. II. Cylindrical geometry," *IEEE Transactions on Medical Imaging*, Vol. 21, No. 7, 829–833, 2002.
12. Xu, Y., D. Feng, and L. V. Wang, "Exact frequency-domain reconstruction for thermoacoustic tomography. I. Planar geometry," *IEEE Transactions on Medical Imaging*, Vol. 21, No. 7, 823–828, 2002.
13. Xie, Y., B. Guo, J. Li, G. Ku, and L. V Wang, "Adaptive and robust methods of reconstruction," Vol. 55, No. 12, 2741–2752, 2008.
14. Eckhart, A. T., R. T. Balmer, W. A. See, and S. K. Patch, "Ex vivo thermoacoustic imaging over large fields of view with 108 MHz irradiation," *IEEE Trans. Biomed. Eng.*, Vol. 58, No. 8, 2238–2246, 2011.
15. Wang, X., D. Bauer, R. Witte, and H. Xin, "Microwave-induced thermoacoustic imaging model for potential breast cancer detection," *IEEE Trans. Biomed. Eng.*, Vol. 06, No. 01, 1350001, 2012.
16. Zhu, X., Z. Zhao, J. Wang, G. Chen, and Q. H. Liu, "Active adjoint modeling method in microwave induced thermoacoustic tomography for breast tumor," *IEEE Trans. Biomed. Eng.*, Vol. 61, No. 7, 1957–1966, 2014.
17. Song, J., et al., "Evaluation of contrast enhancement by carbon nanotubes for microwave-induced thermoacoustic tomography," *IEEE Trans. Biomed. Eng.*, Vol. 62, No. 3, 930–938, 2015.
18. Lou, C., S. Yang, Z. Ji, Q. Chen, and D. Xing, "Ultrashort microwave-induced thermoacoustic imaging: A breakthrough in excitation efficiency and spatial resolution," *Phys. Rev. Lett.*, Vol. 109, No. 21, 15, 2012.
19. Razansky, D., S. Kellnberger, and V. Ntziachristos, "Near-field radiofrequency thermoacoustic tomography with impulse excitation," *Med. Phys.*, Vol. 37, No. 9, 4602–4607, 2010.
20. Nan, H. and A. Arbabian, "Peak-power-limited frequency-domain microwave-induced thermoacoustic imaging for handheld diagnostic and screening tools," *IEEE Trans. Microw. Theory Tech.*, 110, 2017.
21. Wang, K. and M. A. Anastasio, "Photoacoustic and thermoacoustic tomography: Image formation principles," *Handbook of Mathematical Methods in Imaging*, O. Scherzer (ed.), 2011.
22. COMSOL Multiphysics v. 5.2, www.comsol.com. COMSOL AB, Stockholm, Sweden.
23. Maxwell, E., "Conductivity of Metallic Surfaces at Microwave Frequencies," *Journal of Applied Physics*, Vol. 18, No. 7, 629–638, 1947.
24. Hristova, Y., P. Kuchment, and L. Nguyen, "Reconstruction and time reversal in thermoacoustic tomography in acoustically homogeneous and inhomogeneous media," *Inverse Probl.*, Vol. 24, No. 5, 55006, 2008.
25. Chen, G., Z. Zhao, Z. Nie, and Q. H. Liu, "Computational study of time reversal mirror technique for microwave-induced thermo-acoustic tomography," *Journal of Electromagnetic Waves and Applications*, Vol. 22, No. 16, 2191–2204, 2008.
26. Treeby, B. E. and B. T. Cox, "k-Wave: MATLAB toolbox for the simulation and reconstruction of photoacoustic wave-fields," *J. Biomed. Opt.*, Vol. 15, No. 2, 021314, 2010.
27. Kuchment, P. and L. Kunyansky, "Mathematics of photoacoustic and thermoacoustic tomography," *Handbook of Mathematical Methods in Imaging*, 881–865, 2011.
28. Gabriel, C., S. Gabriel, and E. Corthout, "The dielectric properties of biological tissues: I. Literature survey," *Phys. Med. Biol.*, Vol. 41, No. 11, 2231–2249, 1996.